ELSEVIER

Contents lists available at ScienceDirect

Extreme Mechanics Letters

journal homepage: www.elsevier.com/locate/eml





Generative AI model trained by molecular dynamics for rapid mechanical design of architected graphene

Milad Masrouri ^{a,b}, Kamalendu Paul ^{a,b,c}, Zhao Qin ^{a,b,d,*}

- ^a Department of Civil and Environmental Engineering, Syracuse University, Syracuse, NY 13244, USA
- b Laboratory for Multiscale Material Modelling, Syracuse University, 151L Link Hall, Syracuse University, Syracuse, NY 13244, USA
- ^c Department of Physics, Syracuse University, Syracuse, NY 13244, USA
- ^d The BioInspired Institute, Syracuse University, NY 13244, USA

ARTICLE INFO

Keywords: Architected graphene Molecular dynamics Stable Diffusion Low Rank Adaptation Von Mises stress field

ABSTRACT

Generative artificial intelligence (AI) is shown to be a useful tool to automatically learn from existing information and generate new information based on their connections, but its usage for quantitative mechanical research is less understood. Here, we focus on the structure-mechanics relationship of architected graphene as graphene with void defects of specific patterns. We use Molecular Dynamics (MD) to simulate uniaxial tension on architected graphene, extract the von Mises stress field in mechanical loading, and use the results to train a fine-tuned generative AI model through a Low-Rank Adaptation method. This model enables the freely designed architected graphene structures and predicts its associated stress field in uniaxial tension loading through simple descriptive language. We demonstrate that the fine-tuned model can be established with a few training images and can quantitatively predict the stress field for graphene with various defect geometries and distributions not included in the training set. We validate the accuracy of the stress field with MD simulations. Moreover, we illustrate that our generative AI model can predict the stress field from a schematic drawing of the architected graphene through image-to-image generation. These features underscore the promising future for employing advanced generative AI models in end-to-end advanced nanomaterial design and characterization, enabling the creation of functional, structural materials without using complex numerical modeling and data processing.

1. Introduction

2D materials (e.g., graphene, MoS2, Mxene, BN) have ultrathin thickness and remarkable mechanical strength, electrical conductivity, and thermal conductivity in comparison to their 3D bulk form, making them promising materials for future manufacturing in compact size [1–6]. Graphene exhibits high electrical conductivity, with a Young's modulus of 1 TPa and an ultimate mechanical strength of 90 GPa [2]. Its impressive thermal conductivity of 5300 W·m–1·K–1 [7] enables effective performance under extreme mechanical, electrical, and thermal conditions, making it suitable for applications such as batteries, sensors, transistors, and robust composites [8,9]. Research efforts have explored doping methods and material composites to enhance graphene's mechanical strength, often resulting in altered electrical properties. For instance, introducing carbon nanotube (CNT) rebars embedded in graphene has demonstrated a fourfold increase in fracture energy [10]. Conversely, ordered defects in graphene have shown promise in tuning

its mechanics without introducing foreign materials [11]. Previous studies have highlighted the effectiveness of pillared structures in enhancing the flexibility and toughness of 3D-printed macroscopic samples and applying this strategy to graphene and other 2D materials [12]. The introduction of architectural defects in the form of alternative bridge-gap structures has been observed to disperse stress concentrations and enhance both the strength and toughness of 2D materials [9]. It is shown that these mechanical features strongly depend on the stress field of the material subjected to loading.

MD simulations, particularly when executed with precise force fields, yield highly accurate predictions of the mechanical response of nanomaterials, including the atomistic scale molecular behavior level and large-scale stress field [14-16]. However, they are computationally demanding and can easily exceed the available computational capacity if used to produce massive data for brute-force designing and optimization purposes. In contrast, deep learning has arisen as a promising solution for tackling this challenge, offering an alternative to

^{*} Corresponding author at: Department of Civil and Environmental Engineering, Syracuse University, Syracuse, NY 13244, USA *E-mail address*: zqin02@syr.edu (Z. Qin).

first-principle methods like MD or finite element methods (FEM) [17]. It acts as an auxiliary model for MD and FEM by integrating the constitutive relationship and differential equations and simply replacing the correlation functions, which accelerates mechanical behavior prediction [18]. It also enables the massive consideration and comparison of different design configurations and the use of the results to make material design and rational reverse design possible [19]. However, most of these supervised learning methods are limited by the high training data and the quality requirements. They prevent it from being used in research applications because pioneering research usually lacks data, and the available data must be better structured.

Since 2022, artificial intelligence generated content (AIGC) has performed exceptionally well and garnered significant interest from researchers. AI-based image generators, including DALL-E 2 [20], Imagen [21], Midjourney [22], and Stable Diffusion (SD) [23], have emerged as a notable area of study. The main objective of these generative AI algorithms is to create new synthetic images that accurately replicate the patterns found in their training dataset [24]. Among these tools, SD is a generative AI model enabled through image diffusion in the latent space, which facilitates the synthesis of high-resolution images by leveraging perceptual and semantic compressions. This model has proven effective across various applications, including text-to-image [25], text-to-video [26], and super-resolution [27]. Compared to traditional diffusion models [28], SD offers greater computational efficiency, enabling the creation of higher-resolution images. Unlike the original generative adversarial networks (GANs) [29], SD does not suffer from mode collapse or training instabilities. The success of these models suggests the possibility of applying generative AI to process a small amount of data/image and use the augmented data/image for rational design and optimization. While these models have demonstrated their ability to produce realistic images [23,30,31], their potential for material design and characterization remains largely unexplored.

Similar to Large Language Models (LLMs) like GPT by open AI [32], developing special-purpose SD models that are experts in specific tasks or scientific domains can be costly, especially when diverse sets of capabilities are required. However, methods like Low-Rank Adaptation (LoRA) [33], Differential Learning Rates (DLR) [34], Prompt Tuning [35], and Full Model Fine-Tuning [36] have been proposed as a more efficient way to fine-tune a pre-trained model by updating the weights and make the model improve its ability for specific tasks. For example, Buehler has utilized LoRA to fine-tune an LLM, creating MechGPT, which leverages LLMs to improve multiscale modeling of materials failure. [37]. Another fine-tuned LLM, BioinspiredLLM, highlights the potential for AI to accelerate research and scientific discovery in bio-inspired materials [38]. In another study, X-LoRA was presented as a mixture-of-experts, framework enhancing LLMs with LoRAs for specialized tasks in protein mechanics and molecular design [39]. Zhao et al. employed LoRA to train a special-purpose SD model that can efficiently generate remote sensing image-annotation pairs, drastically reducing the time and effort required for detailed pixel-level annotations in semantic segmentation [40]. In our recent research [41], we explored the ability of a fine-tuned SD model to simultaneously generate a bicontinuous composite structure and its corresponding von Mises stress field. We demonstrate that the model is highly data-efficient and successfully captures the essential mechanical characteristics of a bicontinuous composite under load. These studies demonstrate LoRA's effectiveness in fine-tuning general-purpose models into specialized experts focusing on a target scientific domain. LoRA is a training strategy designed to accelerate the training of large models while reducing memory usage, commonly employed for specific, targeted tuning. In LoRA modeling, the principle involves integrating low-rank matrices with the original full-scale matrix, where these low-rank matrices are the sole trainable components of the model. This approach allows the model to retain the extensive knowledge acquired during its initial pre-training phase while adapting more specifically to particular tasks [33].

Here, we establish a workflow that combines Molecular Dynamics (MD) and generative AI enabled through SD to swiftly design the bridge structures for graphene with enhanced toughness and rapidly reveal the stress field of architected graphene under uniaxial load. As depicted in Fig. 1(a), our workflow consists of three primary stages: (I) gathering a training dataset via MD simulations of architected graphene sheets under uniaxial tension, utilizing the resulting von Mises stress fields; (II) fine-tuning a pre-trained SD model using LoRA to tailor it for stress field prediction in architected graphene; and (III) employing the text-to-image and image-to-image capabilities of SD to simultaneously generate 2D graphene sheet configurations with artificially induced defects along with their corresponding von Mises stress fields. Our model can learn the structure-mechanics relationship for the architected graphene sheets and can predict the stress field of an architecture very different from the existing training set (Fig. 1(b)).

2. Materials and method

2.1. MD simulation setup and parameters

We simulate uniaxial strain in architected 2D graphene sheets with a pre-existing sharp crack and periodic artificial defects in front of the crack. The inclusion of a crack in the graphene structure is purposeful to study its impact on stress distribution around defects, specifically focusing on the stress concentration caused by the crack even before it begins to propagate. This detail is crucial for predicting how stress is distributed in the structure with an existing crack, right up to the point where the crack begins to extend. The sample geometry is varied by systematically changing the defect position and dimensions to generate the training data.

The adaptive intermolecular reactive empirical bond order (AIREBO) [42] potential is used to model the interatomic interactions in graphene. Long-range interactions are described by a Lennard-Jones potential with a cutoff of 8.5 Å. The system is energetically minimized using the conjugate gradient method for 20,000 steps with a 1 fs timestep, followed by equilibration to 300 K in the NVE ensemble for 10,000 steps. The fracture is simulated by applying uniaxial strain along the zigzag direction at a rate of 2×10^{-7} Å/fs for 5 ns, with the upper and lower edge atoms fixed. The thickness of graphene is assumed to be 3.35 Å. All simulations are performed using LAMMPS, and OVITO is used to visualize the atomic structures, dynamics, and stress fields. Images portraying the von Mises stress fields at a strain of $\varepsilon = 0.02$, just before crack propagation begins, are processed and collected as the ground truth for the training dataset. The "hot" color map is used for visualizing these stress field contours, which spans from "black" [RGB = (0, 0, 0)], indicating a lower limit stress of 0.2 GPa, to "white" [RGB = (255, 255, 255)], representing an upper limit stress of 50 GPa. Although the specific lower and upper bounds may differ across various cases, they remain uniform within our dataset. Ultimately, the images are saved with a resolution of 1350 \times 2810 pixels. More details about the MD simulation are shown in Fig. S1 in Supplementary Materials and our previous study [13].

2.2. Overall workflow of SD

We employ generative AI enabled through SD models for image generation and fine-tune a pre-trained SD model using the Low Rank Adaptation (LoRA) method, tailoring it specifically for generating architected graphene stress field images.

SD is based on the foundational diffusion approach, specifically denoising diffusion probabilistic models. This method involves two main phases: the forward phase and the backward phase (Fig. 2 (a)). In the forward phase, noise is incrementally added to an original image in a controlled manner, with each step of added noise adhering to a specific normal distribution. This process transforms the original image into one that is completely obscured by noise. During the backward phase, denoising modules that resemble the architecture of a U-Net are trained

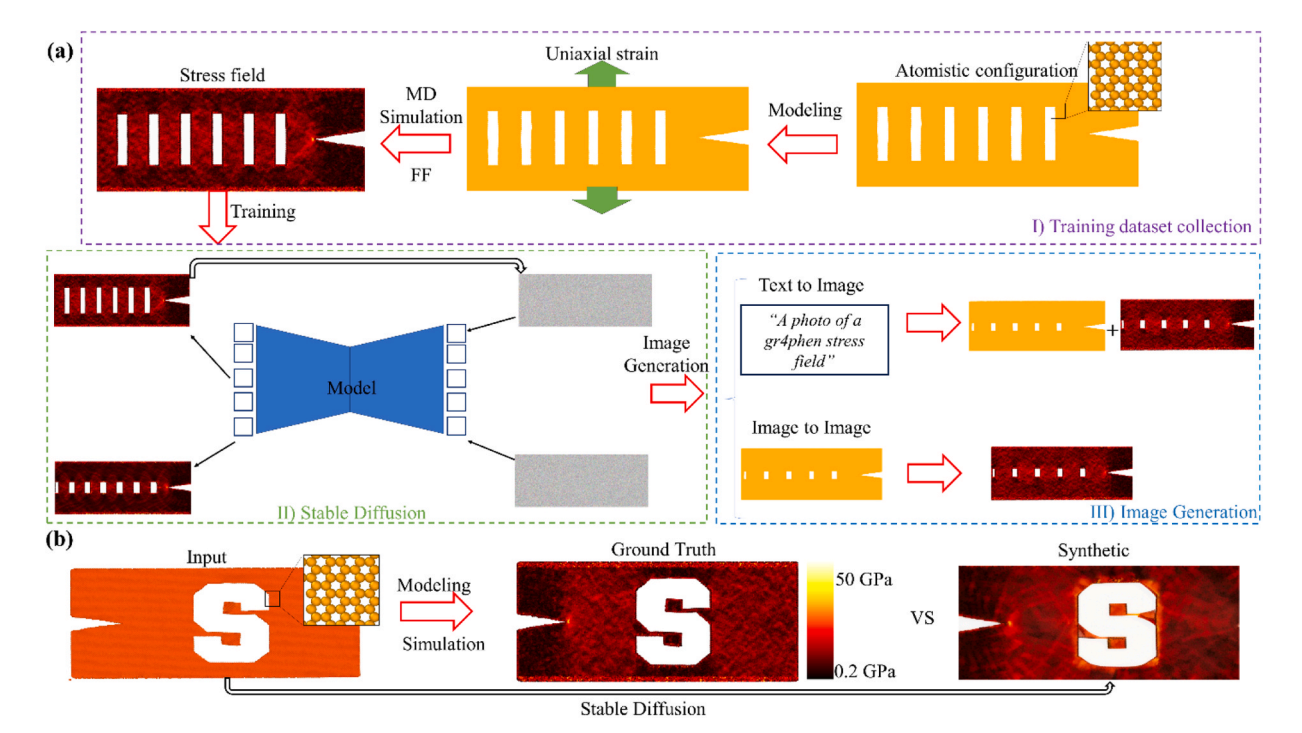


Fig. 1. (a) The overall workflow of the study includes the following: I) training dataset collection, II) generative AI enabled through SD models, and III) image generation. We deliberately modified the spelling of "graphene" to "gr4phen" in the text prompts because we observed that the model showed improved performance by including numbers and special characters. Additionally, this unique phrasing helps distinguish our prompts from those in the pre-existing dataset of the pre-trained SD model. (b) Comparison of the synthetic and ground truth stress field of a graphene configuration that includes a defect in the shape of the Syracuse University logo. This image-to-image generation function underscores the efficiency of this study for designs, which allows bypassing the Molecular Dynamics simulation setup and running it to directly predict the stress field of architected graphene sheets under mechanical loading.

to predict and remove the noise that was added during the forward phase. This denoising process is carried out step by step, starting from the fully noised image and gradually restoring it to resemble the original image. Once the denoising modules are effectively trained, the model can reconstruct images from their noised states, reversing the noise addition process. The general term formula for the forward process can be expressed mathematically:

$$\mathbf{x}_{t} = \sqrt{\alpha_{t}}\mathbf{x}_{t-1} + \sqrt{1 - \alpha_{t}}\varepsilon_{t} \tag{1}$$

Where x_t is the image at timestep t, x_{t-1} is the image at the previous timestep, ε_t represents the noise added at step t, which is sampled from a normal distribution, and α_t is a parameter to describe the noise intensity with $0 \le \alpha_t < 1$. As t increases, more noise is added to x_t , making it less recognizable as the original image x_0 . The entire forward processing can be rewritten as:

$$x_t = \sqrt{\overline{a_t}}x_0 + \sqrt{1 - \overline{a_t}}\epsilon_t \quad , \quad \epsilon_t \quad \in \mathcal{N}(0, I), \quad \overline{a_t} = \prod_{i=1}^t \alpha_i$$
 (2)

The coefficients $\{\alpha_t\}$ are predetermined and its value decreases for each step t, guiding how the original image is gradually converted into a noise-dominated image by the end of the forward process (i.e., $x_t \rightarrow \epsilon_t$). This noised image then serves as the starting point for the backward process, where the model learns to denoise the image step by step, ultimately recovering an approximation of x_0 . In the backward processing phase, under the assumptions of a Gaussian process and Markov chain, the objective is to progressively denoise the image, moving from a state of high noise back to the original or a close approximation of the original image. The mathematical formulation for this process is focused on iteratively estimating and removing the noise added during the forward phase to recover the clean image. The general term formula for the backward process, at a timestep t, can be expressed as:

$$x_{t-1} = \frac{1}{\sqrt{a_t}} \left(x_t - \frac{1 - a_t}{\sqrt{1 - \overline{a_t}}} \epsilon_{\theta}(x_t, t) \right) + \eta_t z_t, \quad z_t \in \mathcal{N}(0, I)$$
 (3)

Where the first term represents the t step recovered image, $\epsilon_{\theta}(x_t,t)$ is the model's estimate of the noise added at time t, that is, the output of the denoising U-Net, $\eta_t = \frac{1-\overline{a}_{t-1}}{1-\overline{a}_t}$ is a parameter controlling the amount of stochasticity or randomness reintroduced at step t, and z_t is a random noise vector sampled from a Gaussian distribution.

In the workflow, the process starts with a stress field image x_0^L . In forward processing, the noise is systematically introduced to x_0^L following Eq. 1 for t times. The culmination of this phase is x_t^L . The backward processing phase begins with x_t^L . The image undergoes a denoising process aimed at restoring it to the original image, x_0^L , by Eq. 3. Once the U-Net is adequately trained to predict and negate the noise, it becomes capable of generating any number of stress field images from a given set of arbitrarily noised images. Fig. 2(a) illustrates the pixel space transformations for clarity. However, most forward and backward processing happens in the latent space.

As illustrated in Fig. 2(b), SD begins by compressing the original image from its pixel format (x) into a more compact latent representation (z) using the encoder ε of a Variational Autoencoder (VAE). The model then undergoes forward processing, resulting in z_T . The model is then refined through backward processing with a denoising U-Net, which aims to remove noise and reconstruct z from z_T . Lastly, the VAE decoder \mathscr{D} translates this refined latent representation (z) back into the original pixel space (\widetilde{x}) , completing the image generation process. The transformer τ_θ encodes the input prompt into a highly informative form for the subsequent image generation steps, ensuring that the final output is a visual representation that matches the prompt's description. Regarding the network details, the diffusion step number t of x_t^L in Fig. 2 (a) is set to 40, implying that the denoising process in the diffusion model is conducted through 40 distinct U-nets in each iteration.

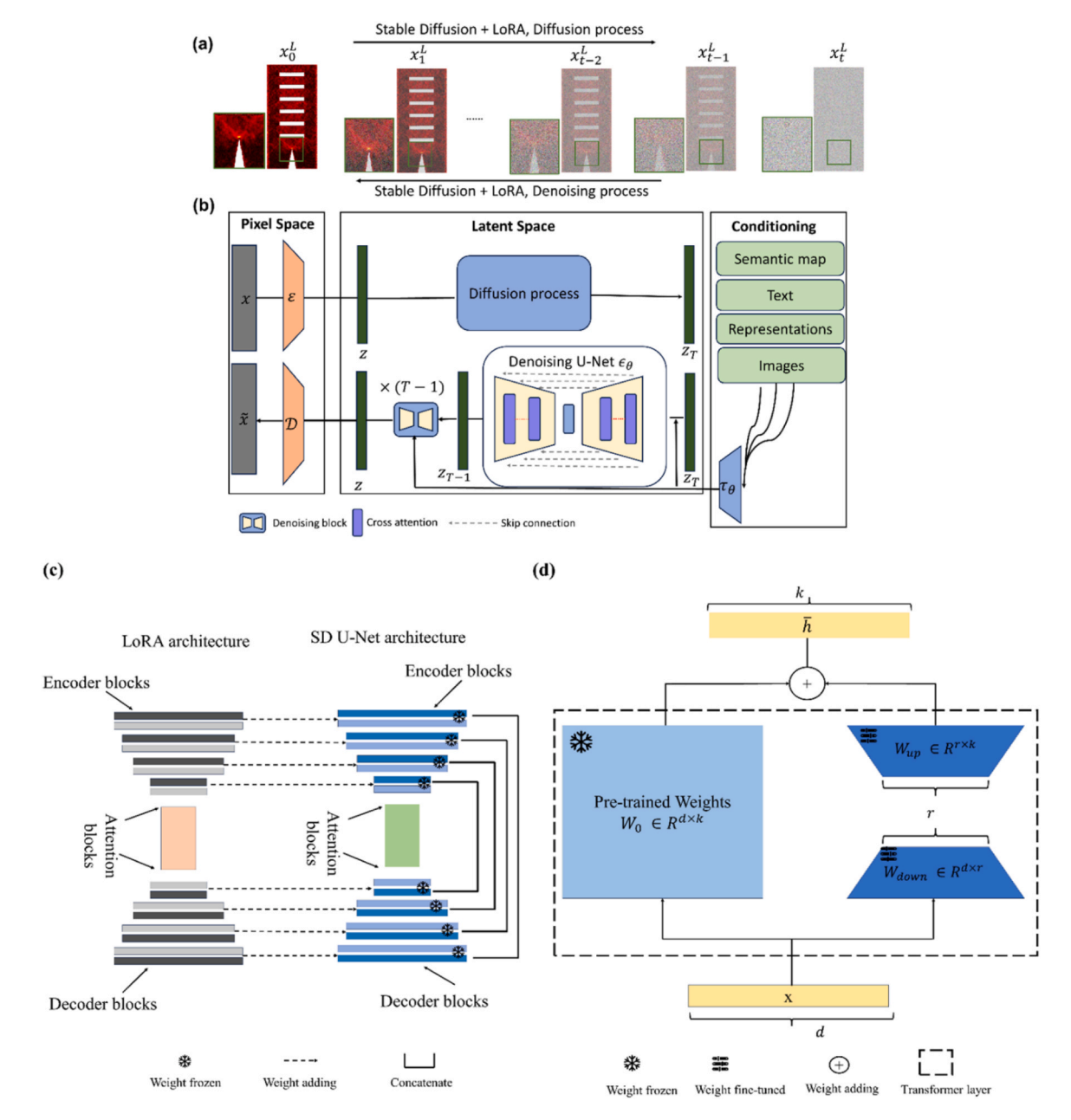


Fig. 2. Overall procedure and network architecture of LoRA-tuned SD model (a)An illustration showing how diffusion and denoising processes are carried out by integrating LoRA and pretrained SD models. The model ultimately learns to create an image from complete noise based on the input text prompt. Although these tasks occur in latent space, they are presented in pixel space for clarity. (b) SD architecture (c) details of SD denoising module and LoRA (d) The core components of LoRA and mechanism of fine-tuning a pre-trained SD model, showing how the weights of the pre-trained model are fine-tuned by LoRA matrices according to Eqs. 4 and 5.

2.3. Technical detail of the LoRA method

To limit the generation of stress field images in the training dataset's pixel distribution and to accelerate the training process, we integrate the LoRA method into a pre-trained model. We apply LoRA to a pre-trained SD model to guide it toward generating the stress field of architected graphene sheets. The LoRA block number is the same as the pre-trained model (Fig. 2(c)). Unlike complete parameter tuning methods that necessitate updating all weights during the fine-tuning phase, LoRA retains the weights of the original model and integrates trainable low-rank matrices to the transformer layers to simulate the weight adjustment. Fig. 2 (d) presents the mechanism of LoRA. Suppose $W_0 \in R^{d\times k}$ as the matrix from the pre-trained model. LoRA approximates the transition from W_0 to $W_0 + \Delta W$ in the following manner:

$$W_0 + \Delta W = W_0 + W_{down} W_{up} \tag{4}$$

Where $W_{down} \in R^{d \times r}$ and $W_{up} \in R^{r \times k}$, with $r^u \min(d,k)$. Wo is held constant throughout the fine-tuning stage, but W_{down} and W_{up} are the adjustable parameters. For any given input x with its original output h, the updated output \overline{h} is calculated as:

$$\overline{h} = W_0 x + \Delta W x = h + W_{down} W_{up} x \tag{5}$$

When fine-tuning the SD model, LoRA can be explicitly employed on the cross-attention layers (Fig. 2 (b) and (c)) that are responsible for establishing connections between image representations and corresponding descriptive prompts.

2.4. Model training

We train five LoRA-tuned SD models using varying numbers of stress field images from our collection pool of 100 architected graphene sheets. Specifically, the models are trained with 10, 20, 40, 80, and 100 images, designated as T10, T20, T40, T80, and T100, respectively. To ensure a robust evaluation and mitigate the influence of selection bias, we employ a randomized selection process to draw images from our training set. Each model undergoes five training iterations (i.e., T10_1, T10_2, ..., T100_5) conducted with different randomly chosen image subsets. Notably, for T100, which utilizes the entire pool of 100 images, variation between iterations arises solely from the sequence in which the images are selected and presented to the model. This methodological approach is designed to rigorously evaluate the impact of training set size on model performance while minimizing potential subjectivity in the selection process.

The selected training images are adjusted to a resolution of $1350\times2810.$ Our training utilizes the stable-diffusion-v1–5 pre-trained model, adopting a batch size of 1, a training duration of 10 epochs, and a learning rate of 0.00001 without any adjustments (constant learning rate schedule). Optimization is performed using the AdamW8bit optimizer, facilitating effective network adjustment. The training hyperparameters are detailed in Table S1 of Supplementary Materials. The training procedure is conducted using the open-source Kohya SS library in Python. We include SAFETENSOR and JSON files for the T100 model in Supplementary Materials to share the model weights and hyperparameters, enabling others to replicate our work effectively.

2.5. Image generation

We employ two distinct approaches to produce stress field images from the trained models: text-to-image and image-to-image translation. A predefined text prompt is the input for the text-to-image approach, guiding the model to generate random stress field images. Subsequently, a binary mask is applied to these images to transform the stress fields into their initial configurations. The image-to-image method uses an initial configuration image as the input, prompting the model to generate a stress field that corresponds directly to the given configuration (Fig. 1(a)). Image generation uses the open-source "Automatic 1111" GUI [43], a user-friendly platform for interaction with the SD model.

2.6. Image normalization and comparison

Using OpenCV, PIL, and NumPy Python libraries, we first convert generated RGB images into grayscale using:

$$\sigma_{\text{gray}} = 0.2989 R_{\sigma_{RGB}} + 0.5870 G_{\sigma_{RGB}} + 0.1140 B_{\sigma_{RGB}}$$
 (6)

Where σ_{gray} is the matrix of pixel values for a grayscale image, and $R_{\sigma_{RGB}}$, $G_{\sigma_{RGB}}$, and $B_{\sigma_{RGB}}$ are the red, green, and blue components of the σ_{RGB} matrix. Next, we normalize σ_{gray} , adjusting pixel values to fall between 0 and 1 using:

$$\overline{\sigma} = \frac{\sigma_{gray} - \min(\sigma_{gray})}{\max(\sigma_{gray}) - \min(\sigma_{gray})}$$
(7)

Then $\overline{\sigma}$ is turned into a 2D configuration through the application of a binary mask combined with a threshold using:

$$\Omega = \begin{cases} 1\&if\overline{\sigma} < \theta \\ 0\&otherwise \end{cases} \tag{8}$$

Where Ω is the matrix of binary configuration, and θ is a defined threshold. These configurations are then subjected to uniaxial strain in LAMMPS (refer to Materials and Methods Section 2.2), and the resulting stress fields are compared to the ground truth images.

To facilitate the comparison and evaluation of the models, we post-process both synthetic and ground truth images. After cropping and resizing to 1350×2810 , we use Eqs. 6 and 7 to obtain $\overline{\sigma}_{synthetic}$ and $\overline{\sigma}_{ground}$ as the normalized pixel value of the generated image and MD output. This step ensures uniformity and enhances contrast. For accuracy assessment, we calculate the Root Mean Squared Error (RMSE) between the ground truth and synthetic images by $\overline{RMSE}_{stress} = \sqrt{\frac{1}{N}\sum_{i=1}^{N}(\overline{\sigma}_{synthetic_i}-\overline{\sigma}_{ground_i})^2}$, where N is the total number of pixels in the images, $\overline{\sigma}_{synthetic_i}$ and $\overline{\sigma}_{ground_i}$ are the pixel values at the i-th position in $\overline{\sigma}_{synthetic}$ and $\overline{\sigma}_{ground}$, respectively. Additionally, the absolute error map is calculated for each pixel to visually highlight discrepancies between the synthetic and the ground truth values. This map effectively summarizes the model's performance by illustrating where and how $\overline{\sigma}_{synthetic}$ and $\overline{\sigma}_{ground}$ differ. The absolute error is computed by $\overline{Error}_{stress} = |\overline{\sigma}_{synthetic}-\overline{\sigma}_{ground}|$.

For image-to-image generation, in addition to the \overline{RMSE}_{stress} and $\overline{Error}_{stress}$, we also calculate $RMSE_{conf}$ and obtain an error map for the generated configurations. This is done by using Eqs. 6–8 to convert a synthetic stress field into a configuration, denoted as $\Omega_{synthetic}$, which is then compared to the input configuration, Ω_{ground} . The RMSE for the configurations is computed using $RMSE_{conf} = \sqrt{\frac{1}{N}\sum_{i=1}^{N} \left(\Omega_{synthetic_i} - \Omega_{ground_i}\right)^2}$, Where N is the total number of pixels in the images, $\Omega_{synthetic_i}$ and Ω_{ground_i} are the pixel values at the i-th position in $\Omega_{synthetic}$ and Ω_{ground_i} , respectively. To visually display discrepancies between the synthetic and ground truth configurations, the formula for computing the absolute error map is given as $Error_{conf} = |\Omega_{synthetic} - \Omega_{ground_i}|$.

Furthermore, we examine how varying the denoising strength, λ , in the SD Image-to-Image tool affects model performance. λ controls the model's alteration of the input image: higher values lead to more significant changes, potentially diverging from the original image to meet the prompt's requirements. In comparison, lower values maintain more of the original features. We quantitatively evaluate the impact of this parameter by calculating \overline{RMSE}_{stress} , $\overline{Error}_{stress}$, $RMSE_{conf}$, and $Error_{conf}$. We maintain a constant Classifier Free Guidance (CFG) scale of 5 to isolate the effects of denoising strength on the model's performance. CFG scale controls the influence of textual prompts on the generated images.

3. Results and discussion

To generate images from the trained SD models, we employ two approaches: 1) text-to-image, where a predefined text prompt acts as the model's stimulus, and 2) image-to-image, in which the model uses a configuration image as input and attempts to predict the stress field of that input based on the associated text prompt (Fig. 1 (a)). For each approach, we evaluate the performance of the prediction with the method, as we discuss in the Materials and Method section.

3.1. Text-to-image generation of architected graphene design and related stress field

We develop five SD models, each comprising five repeats, totaling twenty-five models, as detailed in the Materials and Methods section. While training, we assign each model a unique text prompt, such as "a photo of a graphene stress field" to guide image generation. After training, we assess the models' performance both quantitatively and qualitatively.

3.1.1. Analysis for stress prediction errors and distributions

Fig. 3 compares three synthetic images alongside their actual ground truth counterparts. Our analysis reveals that the models successfully capture key features, including stress concentration at crack tips, stress

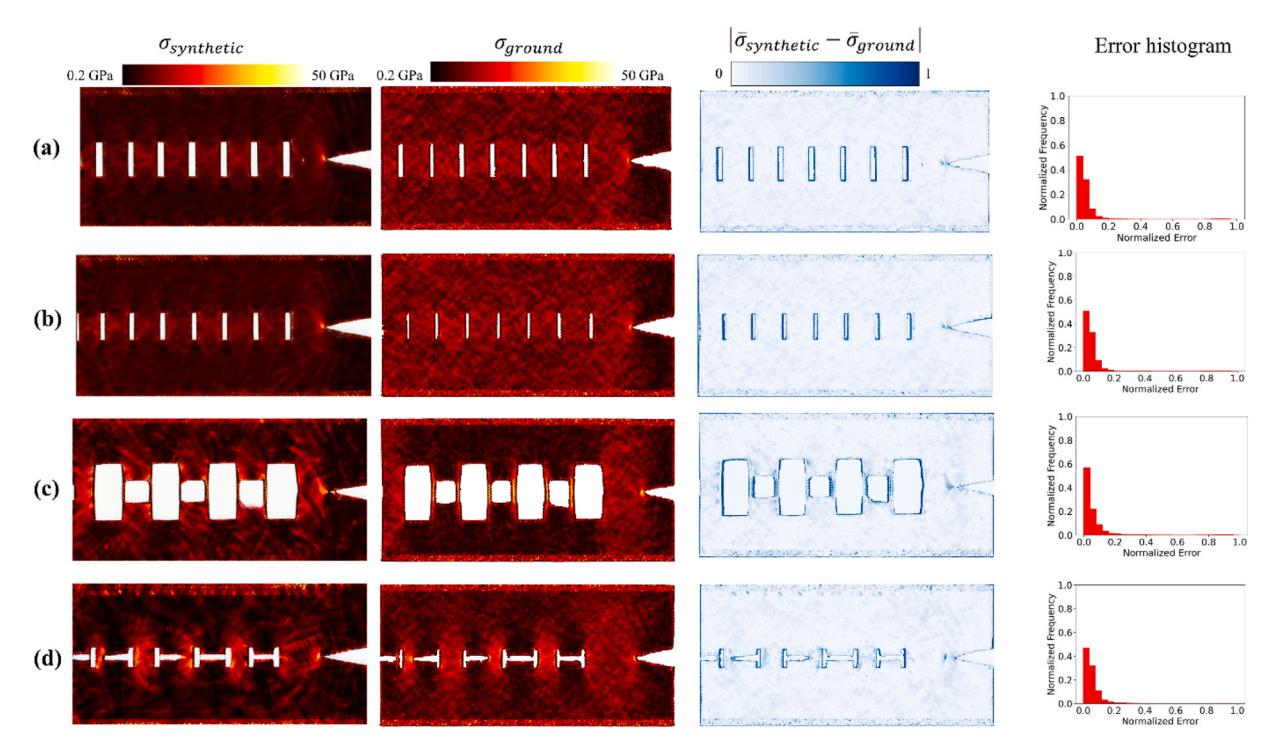


Fig. 3. Comparison between text-to-image synthetic and the corresponding ground truth stress fields. The "Hot" color map is used to visualize the values of von Mises stress. The error map employs a "Blues" heatmap to represent normalized error values, where lighter pixels correspond to lower errors and darker blue pixels indicate higher error magnitudes. The error histogram is derived by computing the ratio of the number of pixels within each bin to the total number of pixels.

distribution near defects, and low-stress areas adjacent to pre-existing cracks. The model also captures the stress drop at the edge, followed by a gradual decrease moving away from the defects (Fig. 3 (a) and (b)). In addition, our methodology adeptly extends beyond the scope of the training data, which consisted of uniform rectangular defects, to accurately predict stress fields in structures with non-uniform rectangular (Fig. 3 (c)) and even diverse defect geometries, such as I-shaped and triangular defects (Fig. 3 (d)). This not only underscores the model's strong capability for generalization but also highlights its proficiency in handling a broad spectrum of novel structural configurations.

Several divergences are evident between the synthetic and ground truth images. In narrow defects, synthetic images often show diminished stress concentrations at the edges compared to ground truth images (Fig. 3 (b)). This contrast arises because, in ground truth data, the proximity of carbon atoms allows for non-bonded interaction between them, thereby sealing the defects and eliminating the lower stress regions apparent in synthetic representations. Moreover, the generated images sometimes fail to accurately represent the stress of the free-hanging atoms near the defects' edges, as seen in Fig. 3(c). The free-hanging carbon atoms effectively feel no stress in the ground truth, which is not the case for some synthetic images generated.

3.1.2. Fine-tuned models for reducing stress prediction errors

The error histograms shown in Fig. 3 have a prominent peak at or near zero, suggesting that most errors in the image comparison are minimal. This peak indicates that the synthetic images closely match the ground truth, with the majority of pixel-wise comparisons yielding minor errors.

Unlike GANs, which are data-intensive and require substantial datasets for training, SD models demonstrate robust performance even with limited training data. We construct our training dataset with only 100 images to emphasize this advantage. To explore the effect of training dataset size on model accuracy, we conduct experiments with subsets of 10,20,40,80 and 100 images. To minimize the subjectivity in selecting training images from the dataset pool, we subject each of the

five models to five separate training runs, each generated by randomly selecting images (refer to Materials and Methods for details). During the image generation, we observe that some models occasionally produce unacceptable images that deviate significantly from expected results, necessitating their rejection. Therefore, we introduce another metric to assess model reliability based on the ability of the models to generate images that meet predefined acceptance criteria—specifically, the presence of a pre-existing crack and at least one structural defect in the generated images. We compute the ratio of accepted images, denoted as P_{accept} , to all generated images to quantify this aspect. (Fig. S2 in Supplementary Materials demonstrates examples of rejected and accepted images). Consequently, we calculate P_{accept} for each model by P_{accept} $\frac{N_{accept}}{N_{bool}}$, where N_{accept} and N_{total} represent the number of accepted and total images for each model, respectively. This approach allows us to quantitatively measure the consistency and reliability of each model in producing images that align with the essential characteristics of the ground truth images. For each iteration, ranging from T10_1 to T100_5, we generate 200 images, resulting in 1000 images per model. We compute P_{accept} for each iteration and then calculate the average P_{accept} across all iterations of a model to determine the P_{accept} of each model. The outcomes are depicted in Fig. 4(a), which illustrates that an increase in the volume of training images enhances the models' reliability. This enhancement is evidenced by a reduction in the number of rejected images, indicating that the models have become increasingly precise in forecasting the general characteristics of the training images.

Fig. 4(b) demonstrates that there is no significant improvement in model performance with an increase in the size of the training images, except for the T100 model, which exhibits a lower RMSE. However, there is a noticeable discrepancy between the mean RMSE and the standard deviation across the iterations for each model, underscoring that the specific images chosen for training can influence the effectiveness of the models. This variance is less pronounced in the T100 model, as it uses the entire pool of 100 images, and the variation between its iterations is attributed solely to the order in which images are fed to the model.

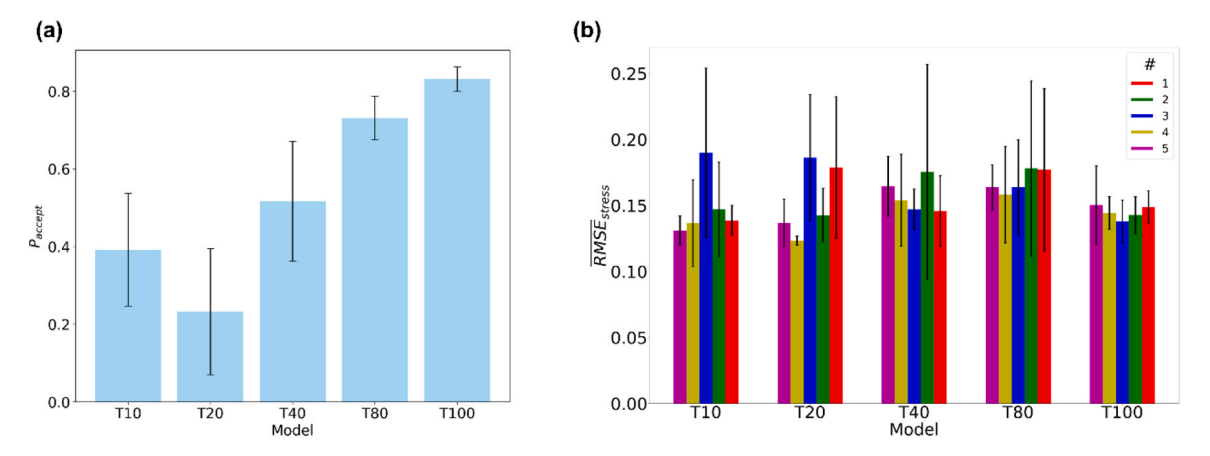


Fig. 4. Effect of training dataset volume on the (a) model's reliability to generate images meeting predefined acceptance criteria and (b) accuracy.

3.2. Image-to-image generation of stress field for a given architecture

We use SD's image-to-image tool to predict the stress field of an input configuration. This feature works by taking the input image and transforming the configuration and color according to the unique textual prompt associated with the model. The output is an image that retains the overall structure of the initial input but is altered in creative ways to reflect the conditions imposed by the textual prompt. Here, we use the T100 model, which best performs in text-to-image comparison.

The results summarized in Fig. 5 illustrate that the image-to-image tool of SD effectively predicts the stress field of specified graphene configurations. Like the text-to-image tool, this method captures critical mechanical attributes within the structure by accurately predicting the associated stress fields. A significant advantage of this tool over the text-to-image option is the ability to control the configuration of the generated structure. Specifically, while the text-to-image tool generates a random structure and its corresponding stress field, the image-to-image tool allows for the input of a predefined structure and the corresponding stress field as the output. This approach is markedly faster than

traditional simulation methods such as FEM and MD, with each image being generated in mere seconds. We further examine the model's generalizability by introducing a graphene configuration that includes a defect in the shape of the Syracuse University logo (Fig. 1(b)). This configuration is entirely novel to the model as it differs from any architected graphene configuration within the training set; nonetheless, it successfully predicts the stress field and identifies the principal structural features. Although the model's performance on this unique configuration is slightly inferior compared to other tested configurations, as depicted in Fig. S4, its ability to delineate major mechanical characteristics within the stress field remains commendable.

The performance of the Image-to-Image tool is significantly influenced by the CFG scale and denoising strength (λ). The CFG scale determines the model's fidelity to the textual prompts during image generation, while λ adjusts the extent to which the model corrects or removes perceived noise during the transformation process, influencing the model's randomness and creativity. By holding the CFG scale constant, we varied λ to observe its impact on the generated configurations and the accuracy of the predicted stress field images. As shown in Fig. 5,

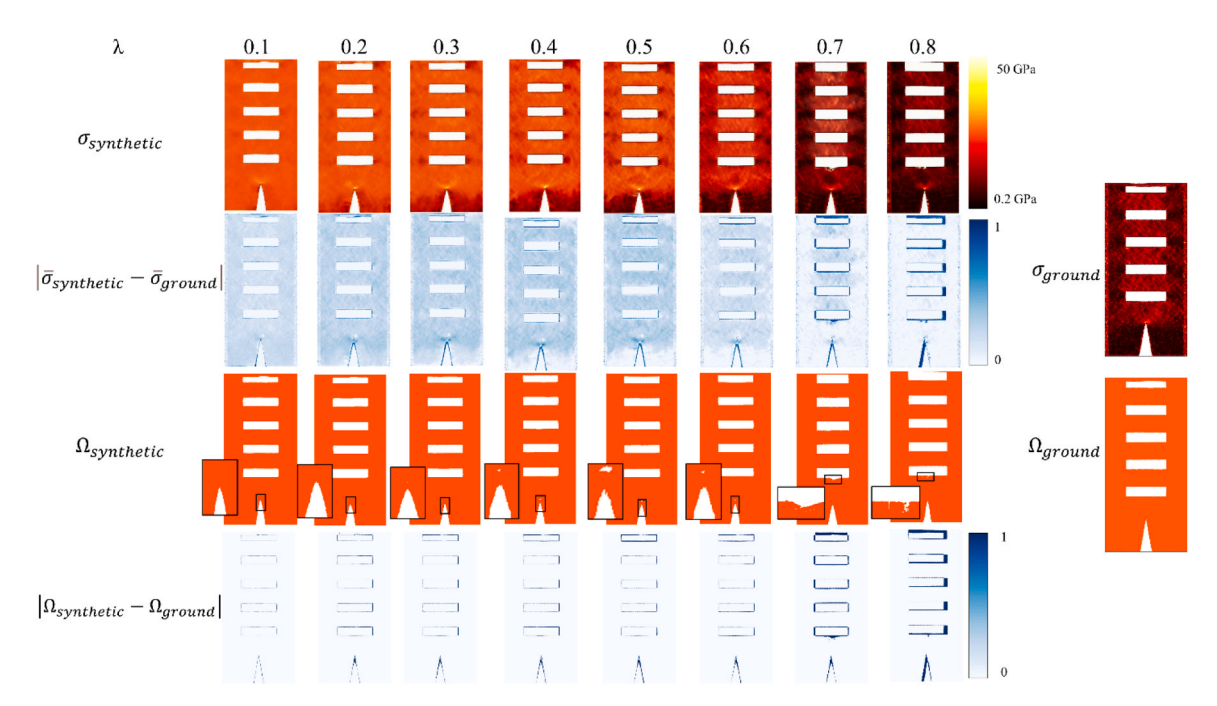


Fig. 5. Performance variation of image-to-image SD models with changing denoising strengths (λ), demonstrating the balance between adherence to input configuration and precision in stress field prediction. The close-up panels in the third row illustrate the increasing divergence of the synthetic configurations from the input as denoising strength increases.

a lower λ value results in the model adhering closely to the input configuration, yet it struggles to predict the stress field accurately. Conversely, increasing λ enhances the model's creativity, allowing it to capture more detailed features in the stress field image, which leads to deviations from the original input configuration. We see the exact influence of λ on the performance of the model for another structure, as shown in Fig. S3. We extend this analysis to 10 different input configurations and calculate \overline{RMSE}_{stress} and $RMSE_{conf}$, which are summarized in Fig. 6. The different overall trends of $RMSE_{conf}$ and \overline{RMSE}_{stress} as functions of λ (Fig. 6 (a) and (b), respectively) suggest a trade-off in model performance influenced by λ . As λ increases, the model diverges from the input configuration, resulting in a rise in RMSE_{conf}. However, the optimal stress prediction, indicated by the lowest \overline{RMSE}_{stress} , is achieved at λ =0.7, as shown in Fig. 6 (b). This reveals a balance between maintaining fidelity to the input configuration and accurately predicting the stress field.

4. Conclusion

In this study, we effectively combined Molecular Dynamics and generative AI techniques, enabled through SD, to design and rapidly predict the stress fields of architected graphene under mechanical load, demonstrating the powerful synergy between these components. By leveraging MD simulations for initial data generation and employing the high-dimensional data-learning capabilities of SD, particularly through LoRA, we have effectively created an AI model to rapidly find and utilize structure-mechanics correlation to design architected graphene structures. We found that for the text-to-image function, by increasing the training dataset volume, the AI model will provide a higher number of reasonable design configurations, and the stress field corresponding to these accepted configurations is more accurate by comparing to MD results. We observed that for the image-to-image function, increasing denoising strength can disrupt the input conformation but provide a stress field with slightly improved accuracy. Our workflow of training and applying the generative AI model to material study can enhance material design efficiency by generating reliable predictions with small data amounts and computational resources. This work underscores the potential of integrating AI in materials science and highlights a promising pathway to create rapid and cost-effective design protocols, which is crucial for application-oriented research.

The architected graphene in this study can be considered an extreme example of composite materials composed of graphene and in-plane voids. Composites of matrix and reinforced components have unique mechanics that outperform each material phase and dominate many modern engineering fields. Classical studies have shown that the composite's toughness can go beyond that of each material phase [44]. Optimizing composite mechanics per se has become a fundamental question: how to decide the material distribution that yields the optimal material functions? Having an efficient tool to facilitate design and reveal the structure-mechanics relationship will help give a quick answer to the question and lead to material innovations for broader engineering applications. Our study demonstrates that outputs of multiscale modeling can finely tune generative AI models. It forms a rapidly evolving technique that can understand and massively produce distinctive designs in response to simple natural language instructions. This tool will, therefore, reduce the technical barrier and computational amount for regular users of numerical modeling. The predicted outcome can be directly applied to composite synthesis for validation or application to broad engineering fields, including aerospace, wind energy industry, high-end automotive, healthcare, sports gear, and construction restoration, by generating coherent designs not limited by human experience or existing models or trapped by local optimal results.

5. Future works

As the future work, our AI model may be enhanced by training generative AI model for movie generation (e.g., Sora by OpenAI) with simulation trajectory that may predict the crack propagation path and its interaction with different architected patterns. At the current point, there are existing works based on CNN to project the crack path and stress-strain curve for a composite design [45,46] despite the limited composite resolution. Laveraging generative AI, we aim to overcome this limitation, significantly increasing the resolution of the composite for which we can predict the mechanical properties and crack propagation path. This approach will also enable us to predict the crack path for architected graphene as well.

Our "text-to-image" model is adept at simultaneously generating novel architected graphene structures and predicting their corresponding stress fields. This capacity to innovate and create designs not encountered during its training underscores GenAI's ability to navigate and expand the design space, while providing critical stress field data for these new configurations. This functionality is integral to the development of pioneering structural designs. Looking ahead, however, we aim to enhance the model's utility by integrating it with deep neural networks (DNN), optimization techniques, and mechanical analysis. These future studies will focus on predicting mechanical properties from the generated structures and their stress fields, and optimizing these

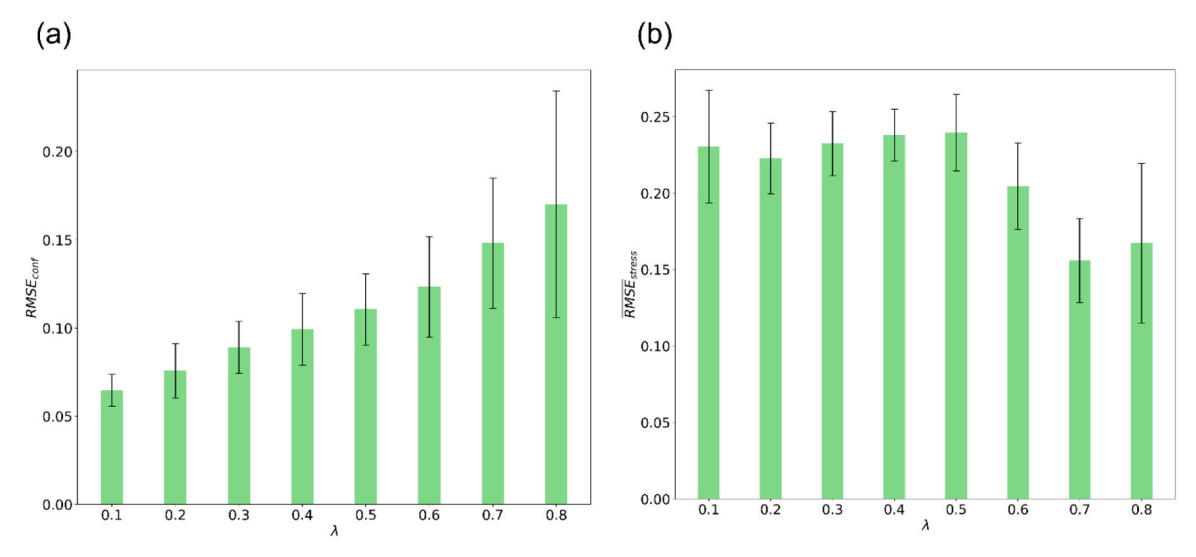


Fig. 6. Impact of denoising strength (λ) on T100 model precision for generating (a) configurations and (b) stress fields in the Image-to-Image generation via SD.

structures to meet specific design targets.

CRediT authorship contribution statement

Kamalendu Paul: Writing - review & editing, Writing - original draft, Visualization, Validation, Data curation. Milad Masrouri: Writing - review & editing, Writing - original draft, Visualization, Validation, Formal analysis, Data curation. **Zhao Qin:** Writing – review & editing, Writing - original draft, Supervision, Software, Resources, Project administration, Methodology, Investigation, Funding acquisition, Conceptualization.

Declaration of Competing Interest

The authors declare no competing financial interest.

Data availability

I have already attached the parameter and model of our study

Acknowledgments

MM and ZQ acknowledge Brodsky's fund at Syracuse University in support of this research work. ZQ acknowledges funding support from the National Science Foundation CAREER Grant (CMMI-2145392).

Appendix A. Supporting information

Supplementary data associated with this article can be found in the online version at doi:10.1016/j.eml.2024.102230.

References

- [1] A.H. Castro Neto, F. Guinea, N.M.R. Peres, K.S. Novoselov, A.K. Geim, The electronic properties of graphene, Rev. Mod. Phys. vol. 81 (1) (Feb. 2009)
- [2] G. Jung, Z. Qin, M.J. Buehler, Molecular mechanics of polycrystalline graphene with enhanced fracture toughness, Extrem. Mech. Lett. vol. 2 (Dec. 2015) 52-59.
- [3] N. Zhang, Y. Hong, S. Yazdanparast, M. Asle Zaeem, "Superior structural, elastic and electronic properties of 2D titanium nitride MXenes over carbide MXenes: a comprehensive first principles study,", 2D Mater. vol. 5 (4) (Jan. 2018) 45004.
- Y. Ibrahim, A. Mohamed, A.M. Abdelgawad, K. Eid, A.M. Abdullah, A. Elzatahry, The recent advances in the mechanical properties of self-standing two-dimensional MXene-based nanostructures: deep insights into the supercapacitor, Nanomaterials vol. 10 (10) (Jan. 2020) 1916.
- [5] J.A. Stewart, D.E. Spearot, "Atomistic simulations of nanoindentation on the basal plane of crystalline molybdenum disulfide (MoS2),", Model. Simul. Mater. Sci. Eng. vol. 21 (4) (Mar. 2013) 45003.
- [6] R. Zahedi, N. Alajlan, H. Zahedi, T. Rabczuk, "Mechanical properties of All MoS2 monolayer heterostructures: crack propagation and existing notch study,", Comput. Mater. Contin. vol. 70 (3) (Jan. 2021) 4635-4655.
- [7] H. Chen, Y. Wen, Y. Qi, Q. Zhao, L. Qu, C. Li, "Pristine titanium carbide MXene films with environmentally stable conductivity and superior mechanical strength,", Adv. Funct. Mater. vol. 30 (5) (Dec. 2020) 1906996.
- [8] C. Lee, X. Wei, J.W. Kysar, J. Hone, "Measurement of the elastic properties and intrinsic strength of monolayer graphene,", Science vol. 321 (5887) (2008)
- [9] K.S. Novoselov, et al., "Two-dimensional gas of massless Dirac fermions in graphene,", Nature vol. 438 (7065) (Dec. 2005) 197-200.
- [10] E.F. Hacopian, et al., "Toughening graphene by integrating carbon nanotubes,", ACS Nano vol. 12 (8) (Dec. 2018) 7901-7910.
- [11] P.Z. Hanakata, E.D. Cubuk, D.K. Campbell, H.S. Park, "Accelerated search and design of stretchable graphene kirigami using machine learning,", Phys. Rev. Lett. vol. 121 (25) (Feb. 2018) 255304.
- [12] S. Heide-Jørgensen, M.K. Budzik, K.T. Turner, "Mechanics and fracture of structured pillar interfaces,", J. Mech. Phys. Solids vol. 137 (Dec. 2020) 103825.
- [13] K. Paul, C.J. Zhang, C.H. Yu, Z. Qin, "Bridged structures in ultrathin 2D materials for high toughness.,", Mech. Mater. vol. 191 (October 2023) (2024) 104932.
- [14] M.J. Buehler, "Atomistic and continuum modeling of mechanical properties of collagen: Elasticity, Fract., self-Assem.," J. Mater. Res. vol. 21 (8) (2006) 1947–1961.

- [15] M. Masrouri, Z. Qin, "Effects of terminal tripeptide units on mechanical properties of collagen triple helices,", Extrem. Mech. Lett. vol. 64 (2023) 102075.
- M. Jiang, C.-H. Yu, Z. Xu, Z. Qin, Binding of carbon monoxide to hemoglobin in an oxygen environment; force field development for molecular dynamics, J. Chem. Theory Comput. (Feb. 2024).
- [17] J. Schmidt, M.R.G. Marques, S. Botti, M.A.L. Marques, Recent advances and applications of machine learning in solid-state materials science, npj Comput. Mater. vol. 5 (1) (2019) 83.
- [18] L. Wang, J. Boddapati, K. Liu, P. Zhu, C. Daraio, W. Chen, Mechanical cloak via data-driven aperiodic metamaterial design, Proc. Natl. Acad. Sci. vol. 119 (13) (Mar. 2022) e2122185119.
- [19] G.X. Gu, C.-T. Chen, M.J. Buehler, De novo composite design based on machine learning algorithm, Extrem. Mech. Lett. vol. 18 (2018) 19-28.
- [20] A. Ramesh, P. Dhariwal, A. Nichol, C. Chu, and M. Chen, "Hierarchical Text-Conditional Image Generation with CLIP Latents," no. Fig. 3, 2022.
- C. Saharia, et al., Photorealistic text-to-image diffusion models with deep language understanding,", Adv. Neural Inf. Process. Syst. vol. 35 (2022).
- [22] J.-R. Anna, "Artificial intelligence as part of future practices in the architect's work: MidJourney generative tool as part of a process of creating an architectural form,", Architectus vol. 3 (71) (2022) 95-104.
- [23] R. Rombach, A. Blattmann, D. Lorenz, P. Esser, and B. Ommer, "High-Resolution Image Synthesis with Latent Diffusion Models," Proc. IEEE Comput. Soc. Conf. Comput. Vis. Pattern Recognit., vol. 2022-June, pp. 10674-10685, 2022.
- [24] G. Zhou et al., "Emerging Synergies in Causality and Deep Generative Models: A Survey," vol. 14, no. 8, pp. 1-22, 2023.
- [25] N. Dehouche, K. Dehouche, What's in a text-to-image prompt? The potential of stable diffusion in visual arts education, Heliyon vol. 9 (6) (Jun. 2023) e16757.
- [26] A. Blattmann et al., "Align Your Latents: High-Resolution Video Synthesis with Latent Diffusion Models," Proc. IEEE Comput. Soc. Conf. Comput. Vis. Pattern Recognit., vol. 2023-June, pp. 22563-22575, 2023.
- J. Ackermann and M. Li, "High-Resolution Image Editing via Multi-Stage Blended Diffusion," 2022.
- [28] J. Ho, A. Jain, P. Abbeel, "Denoising diffusion probabilistic models,", Adv. Neural Inf. Process. Syst., Vol. 2020-Decem, no. NeurIPS 2020 (2020) 1-12.
- [29] S. Zhang, et al., Robust generative adversarial network,", Mach. Learn. vol. 112 (12) (2023) 5135–5161.
- [30] L. Yang et al., "Diffusion Models: A Comprehensive Survey of Methods and Applications," vol. 1, no. 1, 2022.
- [31] Z. Shi, "AI application to generate an expected picture using keywords with stable diffusion, " J. Artif. Intell. Pract. vol. 6 (1) (2023) 66-71.
- [32] H. Fausk, D.C. Isaksen, "Improving language understanding by generative pretraining,", Homol. Homotopy Appl. vol. 9 (1) (2007) 399-438.
- [33] E. Hu et al., "Lora: Low-Rank Adaptation of Large Language Models," ICLR 2022 -10th Int. Conf. Learn. Represent., pp. 1-26, 2022.
- [34] J. Howard and S. Ruder, "Universal Language Model Fine-tuning for Text Classification," 2018.
- B. Lester, R. Al-Rfou, and N. Constant, "The Power of Scale for Parameter-Efficient Prompt Tuning," EMNLP 2021 - 2021 Conf. Empir. Methods Nat. Lang. Process. Proc., pp. 3045-3059, 2021.
- [36] J. Devlin, M.-W. Chang, K. Lee, and K. Toutanova, "BERT: Pre-training of Deep Bidirectional Transformers for Language Understanding," in North American Chapter of the Association for Computational Linguistics , 2019.
- [37] M.J. Buehler, MechGPT, a language-based strategy for mechanics and materials modeling that connects knowledge across scales, disciplines, and modalities, Appl. Mech. Rev. vol. 76 (2) (Jan. 2024).
- [38] R.K. Luu, M.J. Buehler, BioinspiredLLM: conversational large language model for the mechanics of biological and bio-inspired materials, Adv. Sci. vol. 11 (10) (Mar. 2024) 2306724
- [39] E.L. Buehler and M.J. Buehler, "X-LoRA: Mixture of Low-Rank Adapter Experts, a Flexible Framework for Large Language Models with Applications in Protein Mechanics and Design," 2024.
- [40] C. Zhao, Y. Ogawa, S. Chen, Z. Yang, and Y. Sekimoto, "Label Freedom: Stable Diffusion for Remote Sensing Image Semantic Segmentation Data Generation," Proc. - 2023 IEEE Int. Conf. Big Data, BigData 2023, pp. 1022-1030, 2023.
- [41] M. Masrouri, Z. Qin, Towards data-efficient mechanical design of bicontinuous composites using generative AI, Theor. Appl. Mech. Lett. vol. 14 (1) (2024)
- S.J. Stuart, A.B. Tutein, J.A. Harrison, A reactive potential for hydrocarbons with intermolecular interactions, J. Chem. Phys. vol. 112 (14) (Dec. 2000) 6472–6486. [43] AUTOMATIC1111, "Stable Diffusion Web UI." GitHub, 2022.
- U.G.K. Wegst, H. Bai, E. Saiz, A.P. Tomsia, R.O. Ritchie, Bioinspired structural materials, Nat. Mater. vol. 14 (1) (2015) 23-36.
- [45] C. Yang, Y. Kim, S. Ryu, G.X. Gu, Prediction of composite microstructure stressstrain curves using convolutional neural networks, Mater. Des. vol. 189 (2020) 108509.
- J. Lee, D. Park, K. Park, H. Song, T.-S. Kim, S. Ryu, Optimization of grid composite configuration to maximize toughness using integrated hierarchical deep neural network and genetic algorithm, Mater. Des. vol. 238 (2024) 112700.